

First principles electromagnetic responses in medium-mass nuclei

Recent progress from coupled-cluster theory

Johannes Simonis¹, Sonia Bacca¹, and Gaute Hagen^{2,3}

¹ Institut für Kernphysik and PRISMA Cluster of Excellence, Johannes Gutenberg-Universität, Mainz, DE-55128, Germany

² Physics Division, Oak Ridge National Laboratory, Oak Ridge, Tennessee 37831, USA

³ Department of Physics and Astronomy, University of Tennessee, Knoxville, TN 37996, USA

Received: date / Revised version: date

Abstract. We review the recent progress made in the computation of electromagnetic response functions in light and medium-mass nuclei using coupled-cluster theory. We show how a many-body formulation of the Lorentz integral transform method allows to calculate the photoabsorption cross sections of $^{16,22}\text{O}$ and ^{40}Ca . Then, we discuss electromagnetic sum rules, with particular emphasis on the electric dipole polarizability, α_D . By including triples corrections in coupled-cluster theory, we revisit ^{48}Ca , for which, beside the electric dipole polarizability, we had previously investigated the neutron and proton radii, as well as the size of the neutron-skin thickness [1]. We show that correlations among these observables still hold, albeit a better agreement with experiment is obtained for α_D and the prediction of a small neutron-skin thickness is further corroborated.

PACS. 21.60.De Ab initio methods – 24.10.Cn Many-body theory – 24.30.Cz Giant resonances – 25.20.–x Photonuclear reactions

1 Introduction

Electromagnetic probes are invaluable tools to study the nature of composite quantum-mechanical systems, such as nuclei. Due to the small value of the electromagnetic coupling constant α , one can cleanly relate measured cross sections to properties of the composite system via perturbation theory, leading to a more complete understanding of the internal dynamics. Indeed, electromagnetic probes have historically enabled important discoveries regarding the nucleus and the strong dynamics governing its multifaceted properties. Most notably, the study of photonuclear reactions lead to the discovery of giant dipole resonances and to their interpretation in terms of collective modes [2,3]. A complete body of data has been collected over the past decades for stable nuclei, and some selected studies were performed even on unstable nuclei, leading, e.g., to the discovery of pygmy resonances, see, e.g., Ref. [4] and references therein. But where do we stand with the theory today?

One of the goals of modern nuclear theory is to be able to explain nuclear phenomena starting from protons and neutrons as degrees of freedom and by connecting their interactions to quantum chromodynamics via the use of chiral effective field theories [5,6,7,8] or with other more traditional potentials [9]. This research path is called “ab initio approach” in low-energy nuclear physics, see,

e.g., Refs. [10,11,12]. What is meant by that is that, for a given interaction Hamiltonian, the quantum-mechanical problem of protons and neutrons interacting with each other is either solved exactly, or within controlled approximations [13].

In the last years, ab initio computations in nuclear physics have advanced tremendously. While until one or two decades ago it was possible to only deal with very few nucleons, today one can reach even mass number $A \sim 100$ [14,15,16,17] and above. The resulting growth of first principle calculations is well captured in Fig. 1, where we display the trend for ab initio calculations for the nuclear many-body problem as a function of A . In early decades the progress was linear in A , mostly due to exponentially expensive algorithms implemented on machines with exponentially growing computing power. More recently, newly developed polynomial scaling algorithms, such as coupled-cluster theory [18], made it possible to exploit the exponential growth in computing power, pushing the boundaries of first principle calculations. However, one has to note that this fast growing progress regards mostly the computation of bulk properties such as binding energies and radii. Where does this ab initio approach stand with respect to the computation of electroweak reactions with nuclei? Or, in other words, are we able to describe the above mentioned collective modes in a microscopic way, starting from protons and neutrons interacting through realistic forces?

Send offprint requests to:

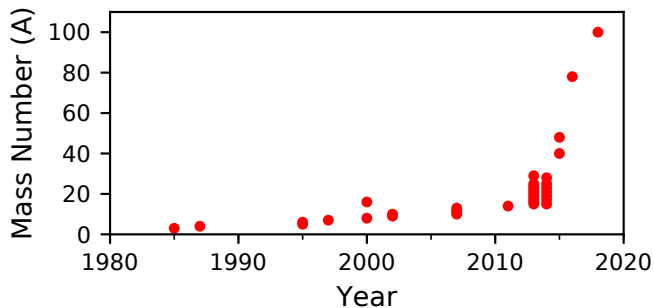


Fig. 1. Trend for realistic first principle calculations for the A -body nuclear problem as a function of A . Figure adapted and updated from Ref. [1].

Only recently we have paved the road to a qualitative and quantitative description of electromagnetic reactions with nuclei from first principles. In this work, we will review the progress made in this respect thanks to the introduction of a new technique obtained by merging coupled-cluster theory [18] with the Lorentz integral transform approach [19,20], that led to a novel computational tool to address electromagnetic reactions and related observables in an ab initio fashion [21].

The paper is structured in the following way. We will first describe the computational tools in Section 2, then, after a brief explanation of the chiral interactions in Section 3, we will present results in Section 4. Finally, we will draw our conclusions and present an outlook for the future in Section 5.

2 Computational tools

2.1 Coupled-cluster theory

Coupled-cluster theory, as originally introduced by Coester and Kümmel [22], is aimed at solving the Schrödinger equation for a many-body system. For a given Hamiltonian \hat{H} describing the quantum system, one assumes that the correlated many-body wave function can be written with an exponential ansatz

$$|\Psi_0\rangle = \exp(\hat{T})|\Phi_0\rangle, \quad (1)$$

where $|\Phi_0\rangle$ is a Slater determinant of any kind. The operator \hat{T} , typically expanded in n -particle- n -hole (np - nh) excitations (or clusters) $\hat{T} = \hat{T}_1 + \hat{T}_2 + \dots + \hat{T}_A$, is responsible for introducing correlations. Using the formalism of second quantization the correlation operators can be writ-

ten as

$$\begin{aligned} \hat{T}_1 &= \sum_{ia} t_i^a \hat{a}_a^\dagger \hat{a}_i, \\ \hat{T}_2 &= \frac{1}{4} \sum_{ijab} t_{ij}^{ab} \hat{a}_a^\dagger \hat{a}_b^\dagger \hat{a}_j \hat{a}_i, \\ \hat{T}_3 &= \frac{1}{36} \sum_{ijkabc} t_{ijk}^{abc} \hat{a}_a^\dagger \hat{a}_b^\dagger \hat{a}_c^\dagger \hat{a}_k \hat{a}_j \hat{a}_i, \\ &\dots \quad \dots \end{aligned} \quad (2)$$

where indices i, j, k, \dots label occupied single-particle (hole) states in the reference Slater determinant, whereas the a, b, c, \dots indicate unoccupied (particle) states.

The many-body Schrödinger equation for the ground state becomes

$$\bar{H}_N |\Phi_0\rangle = E_0 |\Phi_0\rangle, \quad (3)$$

employing the similarity transformed Hamiltonian

$$\bar{H}_N = \exp(-\hat{T}) \hat{H}_N \exp(\hat{T}), \quad (4)$$

where \hat{H}_N is normal ordered with respect to the reference Slater determinant. The amplitudes of the \hat{T} operator, such as t_i^a , t_{ij}^{ab} , t_{ijk}^{abc} , etc., are found by solving the non-linear equations obtained by

$$\begin{aligned} 0 &= \langle \Phi_i^a | \bar{H}_N | \Phi_0 \rangle, \\ 0 &= \langle \Phi_{ij}^{ab} | \bar{H}_N | \Phi_0 \rangle, \\ 0 &= \langle \Phi_{ijk}^{abc} | \bar{H}_N | \Phi_0 \rangle, \\ &\dots \end{aligned} \quad (5)$$

Here, $|\Phi_i^a\rangle$, $|\Phi_{ij}^{ab}\rangle$ and $|\Phi_{ijk}^{abc}\rangle$ are Slater determinants constructed as $1p$ - $1h$, $2p$ - $2h$, $3p$ - $3h$, \dots excitations on top of the reference state, respectively [18,23].

Coupled-cluster theory is exact when the expansion of the \hat{T} operator is performed up to Ap - Ah excitations. However, due to the exponential ansatz of Eq. (11), even when truncations are introduced, the result is very close to the exact one. For closed (sub-) shell nuclei the coupled-cluster method truncated at the $2p$ - $2h$ level, at the so called coupled-cluster singles and doubles level – labeled with D in this work –, captures about 90% of the full correlation energy, while adding triples excitations, about 99% of the correlation energy is accounted for [24,25]. The advantage of the method is that it scales polynomial with increasing system size (by system size we mean a measure of the number of particles and the size of the employed basis). For example, in the D approximation, the algorithm scales as $n_o^2 n_u^4$, where n_o and n_u are the number of occupied and unoccupied orbitals, respectively. Coupled-cluster theory has been successfully applied to study properties of closed (sub-) shell nuclei and their neighbors (see for example Ref. [18] for a review, and references therein).

2.2 Lorentz integral transform method

While enormous progress has been made in first-principles computations of ground-state properties of nuclei with increasing mass number A , advances in the calculation of

electromagnetic reactions with nuclei have been slower, because of the additional challenges one has to face.

Electromagnetic cross sections are typically related to the nuclear response function, defined as

$$R(\omega) = \sum_n |\langle \Psi_0 | \hat{\Theta} | \Psi_n \rangle|^2 \delta(E_n - E_0 - \omega). \quad (6)$$

Here, $|\Psi_0\rangle$ and $|\Psi_n\rangle$ denote ground and final state wave functions of the nucleus, and E_0 and E_n are their respective energies, with $\omega = E_n - E_0$. The operator $\hat{\Theta}$ is a generic electromagnetic operator. One has to note that the \sum_n indicates both the sum over discrete states and an integration over continuum Hamiltonian eigenstates. The calculation of the latter is the main bottleneck in the computation of response functions and thus of electromagnetic cross sections. In particular, the calculation of excited states in the continuum for medium-mass nuclei constitutes an open problem. At a given energy, the wave function is composed by many different channels, corresponding to all possible partitions into different fragments, which are difficult to calculate.

A method that allows to circumvent this issue is the Lorentz integral transform (LIT) [19,20], which reformulates the problem in such a way that the explicit knowledge of all $|\Psi_n\rangle$ in the continuum is not necessary. The Lorentz integral transform is defined as

$$L(\omega_0, \Gamma) = \frac{\Gamma}{\pi} \int d\omega \frac{R(\omega)}{(\omega - \omega_0)^2 + \Gamma^2}, \quad (7)$$

where ω_0 and Γ are parameters, with $\Gamma > 0$. By substituting $R(\omega)$ in Eq. (7) with the expression from Eq. (6) and using the completeness relation of the Hamiltonian eigenstates,

$$\sum_n |\Psi_n\rangle \langle \Psi_n| = 1, \quad (8)$$

one obtains

$$\begin{aligned} L(\omega_0, \Gamma) &= \frac{\Gamma}{\pi} \times \\ &\langle \Psi_0 | \hat{\Theta}^\dagger \frac{1}{\hat{H} - E_0 - \omega_0 + i\Gamma} \frac{1}{\hat{H} - E_0 - \omega_0 - i\Gamma} \hat{\Theta} | \Psi_0 \rangle \\ &= \frac{\Gamma}{\pi} \langle \tilde{\Psi} | \tilde{\Psi} \rangle. \end{aligned} \quad (9)$$

In this way, the LIT of the response function is basically proportional to the squared norm of the state $|\tilde{\Psi}\rangle$. This state is found as solution of the Schrödinger-like equation

$$(\hat{H} - z)|\tilde{\Psi}\rangle = \hat{\Theta}|\Psi_0\rangle, \quad (10)$$

where $z = E_0 + \omega_0 + i\Gamma$, for different values of the parameters ω_0 and Γ . Because of the fact that $L(\omega_0, \Gamma)$ is finite, the unique solution $|\tilde{\Psi}\rangle$ of Eq. (10) has the same asymptotic boundary conditions as a bound state. Thus, only bound-state methods are required to solve this equation.

In the LIT approach one first computes $L(\omega_0, \Gamma)$ in a direct way, without requiring the knowledge of $R(\omega)$. In a

second step, the response function is obtained from a numerical inversion of $L(\omega_0, \Gamma)$ [26,27]. The typical inversion procedure is based on a least-squares fit. First, we make an ansatz for the shape of the response function, e.g., as

$$R(\omega) = \omega^{3/2} \exp\left(-\alpha\pi(Z-1)\sqrt{\frac{2\mu}{\omega}}\right) \sum_i^N c_i e^{-\frac{\omega}{\beta^i}}, \quad (11)$$

where the exponential prefactor is a Gamow factor, assuming that the first channel is the one proton knock out, so that the remaining nucleus has $(Z-1)$ protons. Here $\mu \sim \frac{A-1}{A}m$ is the reduced mass with m being the nucleon mass. The least-squares fit is optimizing the coefficients c_i so that the LIT of Eq. (11) is coinciding with the calculated one. The coefficient β is a non-linear fit parameter which is also varied in the fit procedure. Typically, one can change the ansatz in Eq. (11), vary N and perform the inversion of LITs at different Γ values to obtain an uncertainty of the inversion procedure.

For few-body systems, where a direct calculation of $|\Psi_n\rangle$ even in the continuum case is possible, it has been shown that the LIT method leads to an exact response function [28,29] with the full final state interaction included. Because the relevant equation to solve, Eq. (10), is a bound-state equation, this method essentially circumvents the obstacle of the continuum calculation, the price to pay being that a very good precision in the calculation of $L(\omega_0, \Gamma)$ is needed in order to obtain a stable inversion [20].

The application of the LIT method used in conjunction with hyperspherical harmonics expansions to solve Eq. (10) allowed, e.g., to perform studies of the photodisintegration of the six- and seven-body nuclei [30,31,32].

2.3 Merging coupled-cluster theory with the Lorentz integral transform method

Predictive ab initio calculations of electromagnetic reactions have traditionally been limited to relatively light mass number, as discussed above. Medium-mass and heavy nuclei are typically studied with other theories, such as mean field based approaches and density functional theory [33,34,35,36], which, despite being extremely useful, have a less direct connection to quantum chromodynamics.

To surpass previous limitations of the ab initio approach, we have merged the advantage of the LIT method of reducing the continuum problem to the solution of a bound-state equation with the mild computational scaling that characterizes coupled-cluster theory with increasing mass number. This led to the introduction of a new technique, which we call LIT-CC [21] and which essentially is a coupled-cluster formulation of the LIT method.

Given that in coupled-cluster theory one introduces the exponential ansatz and then one works with similarity transformation, in the LIT-CC method Eq. (10) becomes simply

$$(\bar{H}_N - z)|\tilde{\Psi}_R(z)\rangle = \bar{\Theta}_N|\Psi_0^R\rangle, \quad (12)$$

where $|\Psi_0^R\rangle \equiv |\Phi_0\rangle$ is the right ground state, while $\bar{\Theta}_N$ is the similarity transformed normal-ordered electromagnetic operator

$$\bar{\Theta}_N = \exp(-\hat{T})\hat{\Theta}_N \exp(\hat{T}). \quad (13)$$

The solution $|\tilde{\Psi}_R(z)\rangle$ of Eq. (12) is found as linear superposition of particle-hole excitations on top of the reference Slater determinant as

$$|\tilde{\Psi}_R(z)\rangle = \hat{\mathcal{R}}(z)|\Phi_0\rangle = r_0 + \hat{\mathcal{R}}_1 + \hat{\mathcal{R}}_2 \dots |\Phi_0\rangle,$$

where

$$\begin{aligned} \hat{\mathcal{R}}(z) = & r_0 + \sum_{i,a} r_i^a \hat{a}_a^\dagger \hat{a}_i + \frac{1}{(2!)^2} \sum_{i,j,a,b} r_{ij}^{ab} \hat{a}_a^\dagger \hat{a}_b^\dagger \hat{a}_j \hat{a}_i \\ & + \frac{1}{(3!)^2} \sum_{i,j,k,a,b,c} r_{ijk}^{abc} \hat{a}_a^\dagger \hat{a}_b^\dagger \hat{a}_c^\dagger \hat{a}_k \hat{a}_j \hat{a}_i \end{aligned} \quad (14)$$

$$\begin{aligned} & + \frac{1}{(4!)^2} \sum_{i,j,k,l,a,b,c,d} r_{ijkl}^{abcd} \hat{a}_a^\dagger \hat{a}_b^\dagger \hat{a}_c^\dagger \hat{a}_d^\dagger \hat{a}_l \hat{a}_k \hat{a}_j \hat{a}_i \\ & + \dots \end{aligned} \quad (15)$$

These operators build up particle-hole (p - h) excitations and analogous expressions exist for the bra states.

If the expansions in the \hat{T} and the $\hat{\mathcal{R}}$ operators are performed up to A p - A h , then the theory is exact. However, in practical applications one has to truncate these expansions. The most common approximation is the singles and doubles scheme D, for both the ground state and the excited states. In this work we will investigate different approximation schemes in the ground and excited states. In order to keep the notation concise we therefore denote each scheme with a pair of labels (separated by a ‘/’ symbol), with the largest order of correlation included in the ground state on the left, and the largest order of correlation included in the excited states on the right. For example, when truncating $\hat{T} = \hat{T}_1 + \hat{T}_2$ and $\hat{\mathcal{R}} = r_0 + \hat{\mathcal{R}}_1 + \hat{\mathcal{R}}_2$, we will denote the calculation with D/D.

3 Interactions from χ EFT

In the last decades we have observed the emergence, and its increased application, of chiral effective field theories (χ EFTs) [5,6,7,8] to systematically derive the interactions of nucleons among themselves and with external electroweak probes. This approach allows to maintain a deeper connection to the underlying fundamental theory of quantum chromodynamics (QCD). Effective Lagrangians, expressed in terms of nucleons and pions, are constructed so as to preserve all symmetries, in particular the chiral symmetry, characterizing QCD in the limit of vanishing quark masses. The expansion in powers of $(Q/\Lambda_\chi)^\nu$ is based on a separation of scales, where Q is the low momentum characterizing low energy nuclear physics and $\Lambda_\chi \sim 1$ GeV is the chiral-symmetry breaking scale. The coefficients of the expansion are called Low-Energy Constants (LECs). They encapsulate the unresolved short-range physics and

are adjusted to experimental data. This then makes it possible to predict nuclear observables to any degree ν of desired accuracy, with an associated theoretical error roughly given by $(Q/\Lambda_\chi)^{(\nu+1)}$.

In this approach, see, e.g., Refs. [6,8,7], three-nucleon (3N) forces and higher-body forces arise naturally and consistently with two-nucleon (NN) interactions. As such, they play an important role in consistent calculations. In this paper, we will first show results obtained only with NN forces [37] and then also present results using NN+3N forces. On the one hand we use a set of NN+3N Hamiltonians starting from the next-to-next-to-next-to-leading order (N^3 LO) NN potential of Ref. [37] evolved to lower resolution scales using the similarity renormalization group [38]. These low-momentum interactions are then supplemented with a non-local 3N force at next-to-next-to-leading order (N^2 LO), adjusting the 3N LECs c_D and c_E to reproduce the ^3H binding energy and the ^4He charge radius (for further details see Ref. [39]). On the other hand we use the NNLO_{sat} NN+3N Hamiltonian [40] which was adjusted to reproduce few-body observables as well as binding energies and radii in selected nuclei up to mass number $A \approx 25$. For this latter case, it is to be noted that the NNLO_{sat} potential has been fit to experimental data using the A -CCSD(T) approximation in a model space consisting of 15 oscillator shells and a frequency of 22 MeV. Here, we do not keep these model-space parameters fixed, but vary them in a truly ab initio spirit.

The advantage of using a variety of interactions is that, by doing so, we can give an estimate of systematic uncertainties of the employed Hamiltonians. It also allows us to study whether different observables are correlated, which in turn could be used to make predictions for relevant quantities. Recent examples include the neutron radius and dipole polarizability of ^{48}Ca [1], the 2^+ excited state in ^{78}Ni [14], and electromagnetic transitions in light nuclei [41].

In all the calculations we will show, we use a model-space truncation in N_{max} , the number of harmonic-oscillator shells. While for NN only we reach model-space sizes up to $N_{\text{max}} = 18$, the truncation for NN+3N calculations is $N_{\text{max}} = 14$, if not otherwise specified. Additionally, the 3N matrix elements are truncated in the sum of the three-particle energies with typically $E_{3\text{max}} \leq 16$. The coupled-cluster computations start from a Hartree-Fock reference state. For NN+3N calculations the 3N contributions are included in normal-ordered two-body approximation, discarding residual 3N forces. This approximation is valid for light and medium-mass nuclei as shown in Refs. [42,43].

4 Results

In this section we will present results obtained with the LIT-CC method. We will first focus on the dipole response function and photodisintegration cross section in Subsection 4.1. Then, we will show our studies of sum rules concentrating on the electric dipole polarizability α_D in Subsection 4.2. Finally, we will address the role of triples

corrections in Subsection 4.3 and revisit the correlations among α_D and nuclear radii for ^{48}Ca in Subsection 4.4.

4.1 Dipole response functions

The first electromagnetic reaction observables for which we exploited the power of coupled-cluster theory to address medium-mass nuclei has been the photodisintegration cross section. In the unretarded dipole approximation valid at energies below the pion-production threshold, the photodisintegration cross section can be written as

$$\sigma_\gamma(\omega) = 4\pi^2\alpha\omega R(\omega), \quad (16)$$

where ω is the excitation energy and $R(\omega)$ is the dipole response function, basically Eq. (6) where the electromagnetic operator is the translationally invariant dipole

$$\hat{\Theta} = \sum_k^A (\mathbf{r}_k - \mathbf{R}_{\text{cm}}) \left(\frac{1 + \tau_k^3}{2} \right). \quad (17)$$

Here \mathbf{r}_k and \mathbf{R}_{cm} are the coordinates of the k -th particle and the center-of-mass, respectively, while $(1 + \tau_k^3)/2$ defines the projection operator on the Z protons, with τ_k^3 being the third component of the k -th nucleon isospin.

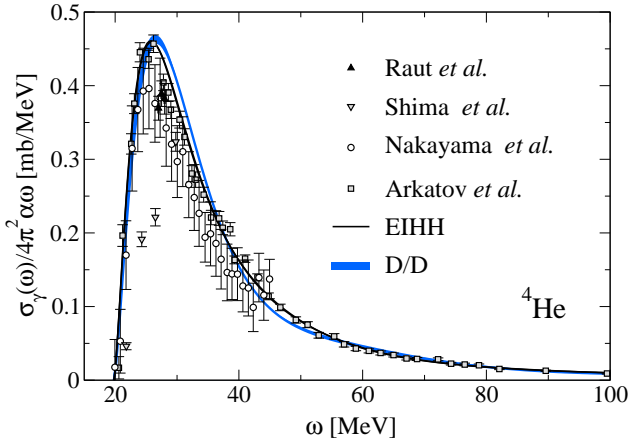


Fig. 2. Dipole response function of the ^4He nucleus. The LIT-CC calculation in the D/D approximation (thick curve) is compared to the exact one (thin curve) obtained from effective interaction hyperspherical harmonics (EIHH). A selected set of the available experimental data is shown for comparison. See text for details.

The photodisintegration cross section of Eq. (16) has been calculated with the LIT method for a variety of light nuclei, from deuteron [28] to ^7Li [32], where the most extensive studies have been performed on ^4He [44]. In these cases the Schrödinger-like equation was solved using exact few-body techniques. Before the new LIT-CC method is

used to study medium-mass nuclei, it is useful to benchmark it against the above mentioned exact calculations. ^4He presents itself as an interesting case study, because it is a closed-shell nucleus, where the LIT-CC method can be most easily applied, and it has been substantially studied both from the theoretical and the experimental point of view. From the theory side, it is particularly instructive to test the D/D approximation against exact calculations performed with effective interaction hyperspherical harmonics [45,46]. In particular, we have performed such a comparison by using a two-body interaction derived in chiral effective field theory at N^3LO [37].

Results of this comparison are shown in Fig. 2, where we present the response function obtained after the inversion of the LIT. In the inversion, we impose the response function to be zero before the threshold energy ω_{th} which is the difference between the binding energy of ^4He and ^3H , with $\gamma + ^4\text{He} \rightarrow ^3\text{H} + p$ being the first open reaction channel in the photodisintegration process. Because, with the N^3LO potential the binding energies of ^4He and ^3H are not correctly reproduced due to the missing 3N forces, a simple way to correct for that is to shift the curves from the theoretical threshold $\omega_{\text{th}} = 17.54$ MeV to the experimental one of 19.82 MeV. In this way, one can focus on the shape of the cross section in the comparison to data. Three-nucleon forces were included, e.g., in Ref. [44], and their effect is to correct the threshold energy and decrease the peak height by a few percent.

The coupled-cluster D/D result is shown by the thick curve. The thickness of the curve is obtained from inverting the LIT with $\Gamma = 10$ MeV and $\Gamma = 20$ MeV and varying N in Eq. (11). The EIHH results are instead represented by the thin curve. In this case, by inverting LITs with $\Gamma = 10$ and 20 MeV, the two results overlap exactly. Interestingly, the D/D response function is close to the EIHH result, proving to be a very good approximation. Only small deviations for energies between about $\omega = 30$ and 50 MeV are seen. These are though much smaller than the uncertainties of most of the experimental data available for the dipole response function.

In Fig. 2, we show a selected set of data for comparison, see Ref. [11] for a more extensive discussion. The Arkatov *et al.* [47] data from the 70s cover the broadest energy range. They are in relatively good agreement with more recent data by Raut *et al.* [48,49], where exclusive experiments were carried out measuring (γ, p) and (γ, n) at the High Intensity Gamma-Ray source. We summed up the two channels and show just the points in the energy range below the three-body break-up. These first two sets of data obtained from traditional photoabsorption experiments, agree rather well with dipole response function data from Nakayama *et al.* [50] obtained via the study of the $^4\text{He}(^7\text{Li}, ^7\text{Be})$ reaction. A completely different trend is instead shown by the Shima *et al.* data from Ref. [51], obtained with a quasi-monoenergetic photon beam and a time projection chamber, where a simultaneous measurement of both the $^4\text{He}(\gamma, n)^3\text{He}$ and $^4\text{He}(\gamma, p)^3\text{H}$ reactions has been performed. Obviously the uncertainties in the experimental data (and the disagreement of about a factor

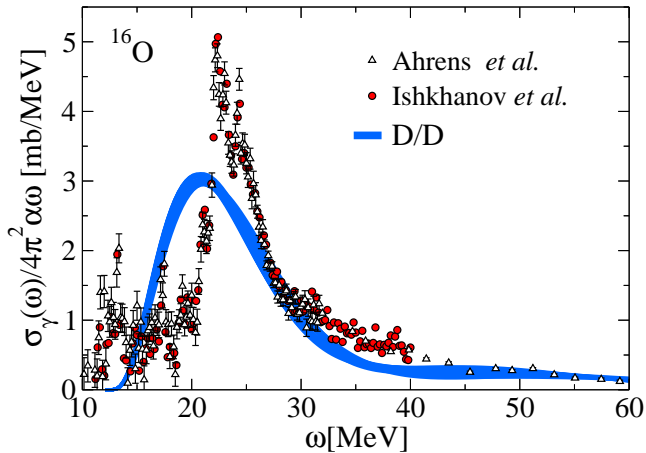


Fig. 3. ^{16}O dipole response function in the D/D scheme calculated with the chiral N^3LO NN force [37] and shifted to the experimental threshold, compared to data from Ahrens *et al.* [52] and Ishkhanov *et al.* [53].

of 2 of the Shima *et al.* data), are much larger than the slight differences we observed between the EIIH and D/D coupled-cluster calculation. We impute this latter difference to the missing triples and quadruple correlations and conclude that they can be safely neglected as their effect is small.

After we successfully benchmarked the new method with exact hyperspherical harmonics on ^4He , we exploit the mild computational scaling of the LIT-CC method with increasing mass number and investigate medium-mass nuclei, for the first time with an ab initio approach.

In Fig. 3, we show the dipole response function of ^{16}O calculated with the LIT-CC method at the D/D approximation level, using the same NN interaction derived in chiral effective field theory at N^3LO [37]. The curve is shown starting from the experimental threshold $\omega_{th} = 12.1$ MeV. The band thickness is obtained by inverting the LIT with width $\Gamma = 10$ MeV and by varying the number of basis functions employed in the inversion. Similar results are obtained by inverting the LIT at $\Gamma = 20$ MeV. We compare the theoretical results with experimental data by Ahrens *et al.* [52], who measured the total photoabsorption cross section σ_γ on an oxygen target with natural abundance (99.762% ^{16}O) with an attenuation method. We also compare to a more recent evaluation by Ishkhanov *et al.* [53]. We observe that the theoretical result is smeared compared to data, but overall the total dipole strength is correctly reproduced, as well as the bulk of the strength is in the right energy range. It is to note though that with this two-body interaction and with the D/D approximation, we do not see the structures at around 10 MeV, which are found in experiment.

Another advantage of coupled-cluster theory is that one can also compute neutron-rich nuclei. In particular, in the oxygen isotopic chain, a few of its neutron-rich iso-

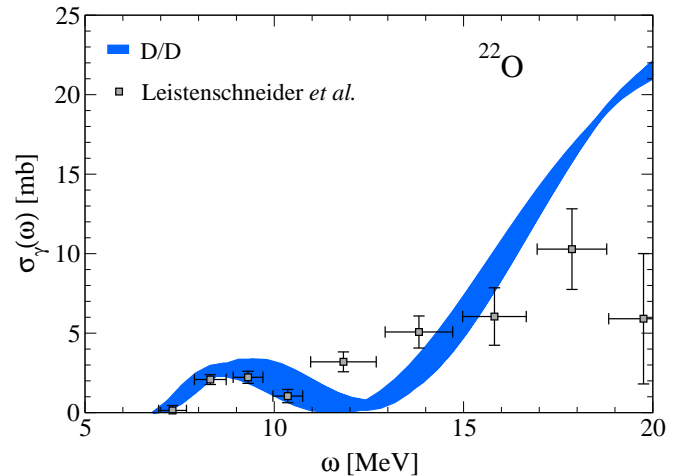


Fig. 4. ^{22}O photodisintegration cross section calculated in the D/D scheme with the chiral N^3LO NN force [37] and shifted to the experimental threshold, compared to data from Ref. [54].

topes have been studied at rare isotope beam facilities. The comparison of stable and unstable nuclei can provide key information about nuclear forces at the extremes of matter. Thus, it is interesting to apply these ab initio methods to exotic nuclei. We will focus on ^{22}O , which is a closed sub-shell nucleus, for which the LIT-CC method can be applied.

In Fig. 4 we show the photoabsorption cross section of ^{22}O computed in the D/D approximation [55] with the chiral N^3LO NN force [37]. The width of the curve is obtained by performing several inversions, for $\Gamma = 20, 10$ and 5 MeV. We compare our results to experimental data taken at GSI by Leistenschneider *et al.* [54]. These are obtained from a Coulomb excitation experiment and are turned into the equivalent of a photoabsorption cross section. The experimental data show a small peak at low energy. This structure is often named pygmy dipole resonance and was experimentally observed in neutron-rich nuclei [4]. Interestingly, our first principle calculation also presents a low-energy peak. The curve is shifted to start from the experimental threshold energy, as done for the other nuclei shown here. We remind the reader that the implemented two-body interaction was tuned only on two-nucleon data. Despite that, we see the emergence of a pronounced substructure at low energy as showed by the data. At higher energies, the D/D results are larger than the data. This is expected because, while the experiment measured a semi-inclusive cross section the theoretical calculation is for an inclusive cross section, where proton emission channels are included.

The heaviest nucleus for which we calculated a response function with the LIT-CC method is ^{40}Ca . In Fig. 5 we show the results in the D/D approximation obtained using the chiral N^3LO NN force [37] used for all other nuclei so far. The width of the curve in Fig. 5 is obtained by

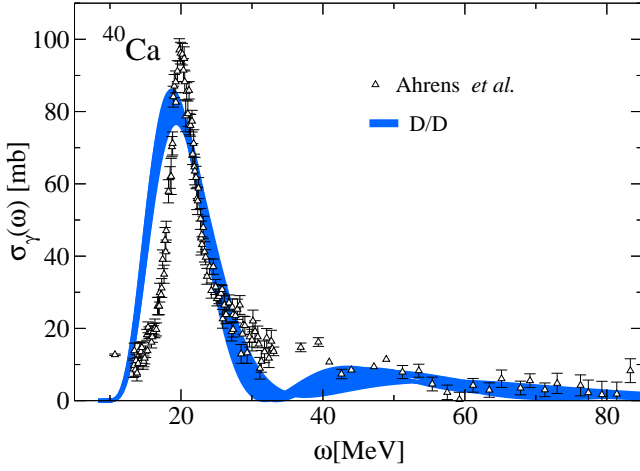


Fig. 5. ^{40}Ca photodisintegration cross section compared to data from Ref. [52]. The curve is calculated with the chiral N^3LO NN force [37] and is shifted to the experimental threshold.

inverting LITs with different Γ parameters. We compare it to the measured cross section by Ahrens *et al.* [52], where a natural calcium target was used with a photoabsorption attenuation method. The data show a very pronounced peak, referred to as the giant dipole resonance and located at an excitation energy of around 20 MeV. This structure is well reproduced by the LIT-CC results.

As mentioned in the Introduction, first interpretations of such resonances, were given in terms of collective models [2,3]. Now, with the advent of novel computational techniques such as the LIT-CC method we are able to show the emergence of these collective modes, both for the giant as well as for the pygmy resonance, from first principles.

Clearly, more work needs to be done to better assess the uncertainties included in the theoretical framework, as well as to include 3N forces. Nevertheless, the results shown in this Section constitute the first successful attempt to describe dipole response functions with ab initio methods. The main difficulty of this approach is that one needs to be able to compute the LIT very precisely, in order to be able to stably invert it. One limiting factor to achieve a sub-percentage convergence in the LIT calculation, is the availability of large model spaces, i.e., of computer memory and of matrix elements of the starting interaction. In all the above shown computations, the precision we could reach employing model spaces of $N_{\text{max}} = 18$ was of the order of one to two percent, and that is the main reason why we obtain quite thick bands in the inversion procedure.

4.2 Electric dipole polarizability

If one is able to calculate the dipole response function, one can then easily compute its existing sum rules as

$$S_n = \int_{\omega_{th}}^{\infty} d\omega R(\omega) \omega^n, \quad (18)$$

where n is an integer number. However, in several instances, it is easier to directly compute some selected sum rules than the whole response function, as the former may be computed as the expectation value of an operator on the ground state.

A particularly interesting sum rule of the dipole response function is the electric dipole polarizability α_D , which is defined as

$$\alpha_D = 2\alpha \int_{\omega_{th}}^{\infty} d\omega \frac{R(\omega)}{\omega}. \quad (19)$$

It is basically an inverse energy weighted sum rule of the dipole response function. As written in Eq. (19), it is evident that α_D contains the information on $R(\omega)$ at all energies ω , including those in the continuum. A calculation of α_D would then require to be able to solve the many-body scattering problem in the continuum or to use alternative approaches as the LIT method. Indeed, for all the nuclei discussed in Subsection 4.1 it is easy to compute α_D by simply performing the integral in Eq. (19).

On the other hand, using the completeness relations it is possible to rewrite α_D as

$$\alpha_D = \langle \Psi_0 | \hat{\Theta}^\dagger \frac{1}{\hat{H} - E_0} \hat{\Theta} | \Psi_0 \rangle. \quad (20)$$

So, if one is able to deal with the operator $\hat{\Theta}^\dagger \frac{1}{\hat{H} - E_0} \hat{\Theta}$, the calculation of α_D reduces to an expectation value of the ground state, where no excited state is involved at all. However, that operator is not easy to write down, so practically what one does is to include completeness of the eigenstates (or a bound-state representation of them) and use an eigenrepresentation of the Hamiltonian. At this point, one can then see a relation between this equation with the second line of Eq. (9). In fact, because in the limit $\Gamma \rightarrow 0$ the Lorentzian kernel becomes a delta function

$$L(\omega_0, \Gamma \rightarrow 0) = \int R(\omega) \delta(\omega - \omega_0) d\omega = R(\omega_0), \quad (21)$$

α_D can be computed from the LIT as

$$\alpha_D = 2\alpha \int \frac{L(\omega_0, \Gamma \rightarrow 0)}{\omega_0} d\omega_0. \quad (22)$$

Equation (21) is nothing else than a discretized response function and Eq. (22) is just an integral of that with an inverse energy weight. In Ref. [56] we showed that this method is equivalent to computing first the response function with the LIT approach and then directly integrate the response function. The advantage of using Eq. (22) is that it does not require to invert $L(\omega_0, \Gamma)$ and have, consequently, an additional numerical error. For this reason,

if one is interested just in the electric dipole polarizability, it is preferable to use this method. In a slightly different spirit, one can understand that it is more complicated to compute the whole response function $R(\omega)$ because knowing the response functions means knowing all of its existing sum rules, not just one.

Table 1. List of results with NN+3N Hamiltonians [39,40] for the charge radius and the electric dipole polarizability for ^{16}O and ^{40}Ca in the D/D approximation. For the notation of the potentials we follow Ref. [39]. Experimental values are taken from Ref. [58] (radius) and Ref. [52,59,60] (electric dipole polarizability).

^{16}O		
Interaction	R_{ch} [fm]	α_D [fm ³]
2.0/2.0(EM)	2.62	0.46
2.0/2.0(PWA)	2.74	0.54
1.8/2.0(EM)	2.60	0.44
2.2/2.0(EM)	2.63	0.48
2.8/2.0(EM)	2.67	0.52
NNLO _{sat}	2.71	0.58
Experiment	2.6991(52) [58]	0.58(1) [52] 0.568(9) [59]
^{40}Ca		
2.0/2.0(EM)	3.35	1.67
2.0/2.0(PWA)	3.55	2.03
1.8/2.0(EM)	3.31	1.57
2.2/2.0(EM)	3.38	1.75
2.8/2.0(EM)	3.44	1.94
NNLO _{sat}	3.48	2.08
Experiment	3.4776(19) [58]	2.23(3) [52] 1.87(3) [60]

The $L(\omega_0, \Gamma)$ in the LIT-CC approach is always computed using the Lanczos algorithm for non-symmetric matrices [55] and in Ref. [56] we showed that α_D can be computed as continued fraction of the Lanczos coefficients [57]. With this technology at hand, we can now explore the dependence of the polarizability on the employed nuclear interaction. For this purpose, we will also use the potentials and normal-ordered 3N forces introduced in Section 3. For the notation of the potentials we follow Ref. [39].

In Table 1 we show results obtained within the D/D approximation for the nuclear charge radius R_{ch} and for α_D for ^{16}O and ^{40}Ca . Calculations were performed with a model-space size of $N_{\text{max}} = 14$, for which we show the central value obtained with the optimal harmonic-oscillator frequency. The uncertainty associated with these D/D calculations were estimated to be of about 1% for the radius and 2% for the polarizability [56].

One can readily see that, as expected, α_D and R_{ch} are strongly correlated. At the bottom of the table we also show the experimental results from Angeli and Marinova [58] for the radius and from Ahrens *et al.* [52] for the polarizability. When integrating the experimental cross section from Ahrens *et al.* [52], a lower value for the polarizability was obtained in Refs. [59,60]. The agreement with

data is particularly good for the interaction NNLO_{sat}, obviously so for the radius of ^{16}O , since it was fit to reproduce the experimental value, while the polarizability and both observables for ^{40}Ca are predictions of this potential. As shown in Ref. [56], if one used two-body forces only, one would still see a strong correlation, but generally an underestimation of the experimental value for both the charge radius and the polarizability.

We remind the reader that, while in Ref. [56] we were able to compute the full $L(\omega_0, \Gamma)$ and invert it for ^4He and ^{16}O with the NNLO_{sat} potential, the inversion procedure was found to be much more unstable than for the calculations with two-body forces only shown in Subsection 4.1, primarily due to the fact that we are limited in the model-space size to about $N_{\text{max}} = 14$ (as opposed to $N_{\text{max}} = 18$ for two-body forces alone), which translate in a larger uncertainty in the $L(\omega_0, \Gamma)$ and consequently on the inversion. Thus, from now on, we will continue our discussion on the electric dipole polarizability only.

4.3 Adding coupled-cluster triples corrections

Coupled-cluster theory is a systematically improvable method. So far we showed results obtained within the coupled-cluster singles and doubles approximation and have assessed uncertainties due to the model-space expansion and residual dependence on the harmonic-oscillator frequency, and by comparing to exact results in light nuclei [1,40]. In order to improve the results and more rigorously assess the uncertainty associated to the coupled-cluster expansion, the next natural step is to include triples corrections. We include leading-order $3p$ - $3h$ excitations using the so called CCSDT-1 iterative triples approach [61] which is a good approximation to the full triples. In the ground state, it typically accounts for about 99% of the correlation energy and includes the leading-order contribution $(\hat{H}_N \hat{T}_2)_C$ (here the index C denotes connected terms [23]) to the \hat{T}_3 amplitudes with an energy denominator given by the Hartree-Fock single-particle energies, while all \hat{T}_3 contributions to the \hat{T}_1 and \hat{T}_2 amplitudes are fully included. We also solve for the corresponding left ground state in the CCSDT-1 following Ref. [62]. Here, we denote this approximation with T-1, consistently with Ref. [59]. Analogously, for the equation of motion and excited states we will add leading-order $3p$ - $3h$ excitations in the T-1 approach [62,63]. When T-1 is used both in the ground state and excited states, we will denote this scheme as T-1/T-1.

When including \hat{T}_3 contribution in the similarity transformation of a normal-ordered one-body operator $\hat{\Theta}_N$ one has

$$\begin{aligned} \bar{\Theta}_N &= \left[\hat{\Theta}_N \exp(\hat{T}_1 + \hat{T}_2 + \hat{T}_3) \right]_C = \\ &= \bar{\Theta}_N^D + \left[\hat{\Theta}_N \left(\frac{\hat{T}_2^2}{2} + \hat{T}_3 + \hat{T}_1 \hat{T}_3 \right) \right]_C, \quad (23) \end{aligned}$$

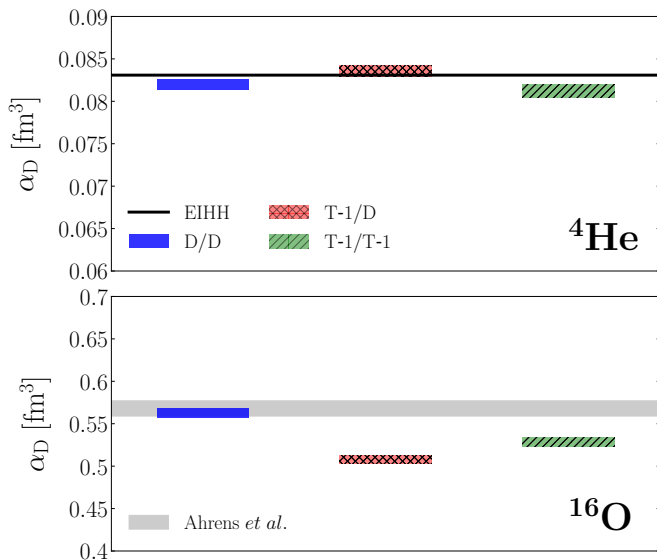


Fig. 6. Electric dipole polarizability for ${}^4\text{He}$ (upper panel) and for ${}^{16}\text{O}$ (lower panel) computed in the D/D (blue/left), the T-1/D (red/central) and the T-1/T-1 (green/right) approximations. For ${}^4\text{He}$ the two-body force from Ref. [37] is used and compared against the exact EIHJ result. For ${}^{16}\text{O}$ we use the NNLO_{sat} Hamiltonian [40] with $N_{max} = 12$ and compare to what we obtain by integrating the experimental cross section from Ahrens *et al.* [52].

where $\bar{\Theta}_N^D$ is the similarity-transformed operator in the D approximation. In Ref. [59] we have shown that $\bar{\Theta}_N$ can safely be approximated with $\bar{\Theta}_N^D$, dramatically simplifying the calculations. Thus, we will only report on results obtained in this scheme.

At this point, it is interesting to compare calculations for the electric dipole polarizability with triples with those only including singles and doubles. Furthermore, because in the computation of α_D we need to specify an approximation scheme for the ground state and for the excited states, we also explore the case where T-1 triples are included only in the ground state, and denote this scheme with T-1/D. Obviously, this calculation is less computationally intensive than the T-1/T-1 case.

In Fig. 6, we show α_D for ${}^4\text{He}$ and ${}^{16}\text{O}$ with the D/D, T-1/D and T-1/T-1 schemes. We employ the chiral two-body force at N³LO from [37] for ${}^4\text{He}$ because we want to benchmark the various approximation schemes against virtually exact EIHJ, which cannot easily employ the NNLO_{sat} Hamiltonian due to the non-locality of the 3N forces. For ${}^{16}\text{O}$ instead we use the NNLO_{sat} Hamiltonian [40], since our goal is to compare with experimental data from Ahrens *et al.* [52].

For ${}^4\text{He}$ we see that the T-1/D calculation agrees best with the hyperspherical harmonics result shown by the black line, surprisingly better than the T-1/T-1 approach. The width of the bands reflects the residual harmonic-oscillator dependence for the largest model space $N_{max} = 14$ and no cut has been done on the $3p-3h$ configurations.

Overall, the effect of $3p-3h$ excitations in ${}^4\text{He}$ is small, at the level of 1 %, which is comparable to the uncertainty obtained from the model-space variation and dependence on the harmonic-oscillator frequency.

For ${}^{16}\text{O}$, while the D/D value is obtained at $N_{max} = 12$, when adding $3p-3h$ configurations we used a model space of $N_{max} = 12$ and $E_{3max}^F = 14$ for T-1/T-1 and T-1/D. Here, E_{3max}^F is an energy cut on the allowed $3p-3h$ excitations, defined as $|N_a - N_F| + |N_b - N_F| + |N_c - N_F| \leq E_{3max}^F$ and $|N_i - N_F| + |N_j - N_F| + |N_k - N_F| \leq E_{3max}^F$ with a given harmonic-oscillator shell N_p and the harmonic-oscillator shell at the Fermi surface N_F . The bands are obtained by assigning a 2% uncertainty, accounting for the combined uncertainty from the E_{3max}^F cut and the residual harmonic-oscillator dependence. Correlations arising from $3p-3h$ excitations reduce the size of α_D , in this case both for T-1/T-1 and T-1/D, by 8% and 10%, respectively. Interestingly, T-1/T-1 and T-1/D are very close to each other showing that including triples corrections into the ground state is more important than including them in the excited states. The few percent difference between the T-1/D and T-1/T-1 results can be taken as an estimate of neglected higher-order correlations. In comparison with the experimental data from [52] shown by the grey band, we see that the addition of triples leads to a further deviation of α_D with respect to the experimental data, which agreed better in the D/D approximation for this interaction. While the comparison to experiment has to be seen as a judgment on the Hamiltonian itself, one also has to keep in mind that the experimental value has been extracted from sum rules from photoabsorption data that may be prone to larger systematic uncertainties than those quoted, because it is difficult to estimate the role of multipoles beyond the dipole.

Table 2. Effect of triples corrections for α_D of ${}^{16}\text{O}$ in fm³ using various NN+3N Hamiltonians [39,40]. For the notation of the potentials we follow Ref. [39]. The experimental value is taken from Refs. [52,59].

${}^{16}\text{O}$		
Interaction	D/D	T-1/D
2.0/2.0(EM)	0.46	0.42
2.0/2.0(PWA)	0.54	0.48
1.8/2.0(EM)	0.44	0.41
2.2/2.0(EM)	0.48	0.43
2.8/2.0(EM)	0.52	0.45
NNLO _{sat}	0.58	0.50
Experiment	0.58(1) [52]	
	0.568(9) [59]	

In Table 2 we include new results for ${}^{16}\text{O}$ obtained within the T-1/D scheme for the electric dipole polarizability, computed with all the Hamiltonians as in Table 1. Interestingly, we find that with triples corrections our results compare better with the value of 0.4959 fm³ obtained by Raimondi and Barbieri [64] with the self-consistent Green's function method for the same NNLO_{sat}

interaction. This might be coincidental as explained in Ref. [59], since coupled-cluster theory in the simple D/S approximation also yields a similar value, namely 0.503 fm^3 . Overall, we find that the effect of coupled-cluster triples corrections is lower for the softer interactions and higher for harder interactions, reaching about 15% for the NNLO_{sat} case. For all the interactions, we get values that slightly under-estimate the experimental data, which as mentioned before, could potentially also include the effect of higher multipoles.

4.4 Revisiting correlations in ^{48}Ca

Recently, the first ab initio computation of the dipole polarizability and the neutron-skin thickness of ^{48}Ca were provided [1]. ^{48}Ca is a neutron-rich isotope of calcium, with 20 protons and 28 neutrons. Despite the fact that it is one of the candidates for neutrino-less double beta decay, its half life is so long, that it can be considered as a stable nucleus and studied in fixed target experiments. In particular, an important observable that is of great interest is the so-called neutron-skin thickness, which is defined as the difference of the root mean square distribution of neutrons, R_n , and of protons, R_p , in the nucleus as

$$R_{\text{skin}} = R_n - R_p. \quad (24)$$

The neutron-skin thickness basically measures the extent of the neutron distribution in a nucleus. While nuclear charge (thus proton) distributions are traditionally easily measured, e.g., with elastic electron scattering, the distribution of neutrons is much more elusive and difficult to access directly. Presently, the cleanest way to measure this quantity is expected to be parity violating electron scattering, which is mediated by the weak force through the exchange of a Z^0 boson. Due to the fact that the proton-weak current is approximately zero, this probe is very sensitive to the location of the neutrons. There are plans to measure neutron skins at Jefferson Laboratory with the CREX [65] and PREX experiments [66], as well as in Mainz with the MREX n-skin project @MESA [67].

In Ref. [1] a study of the correlations of α_D with R_n and R_{skin} was presented, that provided theoretical predictions for all the three above mentioned quantities targeted by modern experiments. The electric dipole polarizability of ^{48}Ca was indeed recently measured with (p, p') reactions in Osaka and was found to be in rather good agreement with coupled-cluster calculations [60], albeit somewhat smaller.

The radii and polarizability calculations in Refs. [1] were performed in the D/D scheme. Here, we revisit our results using the recently developed $3p\text{-}3h$ technology [59]. In Ref. [59] we already computed α_D for ^{48}Ca in the T-1/D scheme for a couple of interactions and found that its values is reduced, improving the agreement with the experimental measurement by Birkhan *et al.* [60]. Here, we supplement our results with a few more Hamiltonians and present complete results for radii and the dipole polarizability in Table 3 (with an increased number of decimal

Table 3. Effect of triples corrections in ^{48}Ca for R_p , R_n , R_{skin} in fm and α_D in fm^3 using various NN+3N Hamiltonians [39,40] as in Table 2. Calculations were performed for the harmonic-oscillator frequency of $\hbar\omega = 16 \text{ MeV}$.

$^{48}\text{Ca}, R_p$		
Interaction	D	T-1
2.0/2.0(EM)	3.271	3.296
2.0/2.0(PWA)	3.502	3.530
1.8/2.0(EM)	3.225	3.247
2.2/2.0(EM)	3.307	3.332
NNLO _{sat}	3.431	3.453
$^{48}\text{Ca}, R_n$		
Interaction	D	T-1
2.0/2.0(EM)	3.423	3.445
2.0/2.0(PWA)	3.656	3.681
1.8/2.0(EM)	3.375	3.395
2.2/2.0(EM)	3.461	3.483
NNLO _{sat}	3.571	3.587
$^{48}\text{Ca}, R_{\text{skin}}$		
Interaction	D	T-1
2.0/2.0(EM)	0.151	0.149
2.0/2.0(PWA)	0.154	0.150
1.8/2.0(EM)	0.150	0.148
2.2/2.0(EM)	0.154	0.151
NNLO _{sat}	0.139	0.134
$^{48}\text{Ca}, \alpha_D$		
Interaction	D/D	T-1/D
2.0/2.0(EM)	2.118	1.952
2.0/2.0(PWA)	2.693	2.414
1.8/2.0(EM)	1.979	1.860
2.2/2.0(EM)	2.233	2.021
NNLO _{sat}	2.645	2.259

digits compared to the other tables in this work for clarity of the following discussion). On the one hand, we find that triples corrections only mildly affect the calculations of R_p and R_n , leading to an increase in both quantities of less than 1%. Triples effects are slightly larger on R_p than on R_n , and as a consequence R_{skin} calculated in the T-1/D scheme is smaller than R_{skin} calculated in the D/D approximation. On the other hand, triples correlations affect α_D quite visibly, as already pointed out in Ref. [59]. In particular, for the harder interactions, their effect is of about 15%.

In Fig. 7 we plot these results, showing the proton radius as a function of the skin radius, the neutron-distribution radius and the electric dipole polarizability. The squares correspond to coupled-cluster calculations in the T-1/D scheme using four different parameterization of the χEFT interactions [39], while the circles correspond to the results obtained with the NNLO_{sat} [40] potential. Each theory point is plotted with error bars that include both the residual $\hbar\omega$ -dependence, as well as an estimate of the coupled-cluster truncation error. Below we briefly explain the recipe we use to estimate uncertainties.

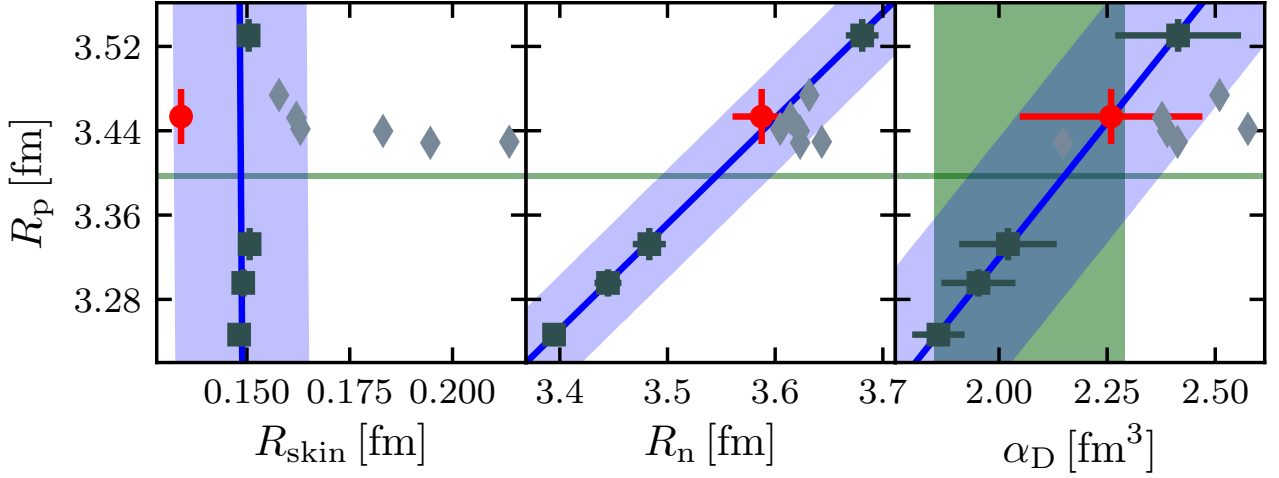


Fig. 7. ^{48}Ca proton-distribution radius versus neutron-skin thickness (left panel), neutron-distribution radius (middle panel), and electric dipole polarizability (right panel). Results include leading triples excitations in coupled-cluster theory and are obtained by using various parameterization of the χEFT interactions [39] (squares) and the NNLO_{sat} (circle) [40] potential. The correlation among these points are indicated by the (blue) light bands, while the experimental values for R_p [58] and α_D [60] are indicated with the (green) darker bands. The diamonds correspond to the selected density functional theory calculations as also shown in Ref. [1].

The uncertainty $\delta_{\mathcal{O}}$ for any observable \mathcal{O} ($R_p, R_n, R_{\text{skin}}$ and α_D) is computed as the quadrature of

$$\delta_{\mathcal{O}} = \sqrt{(\delta_{\mathcal{O}}^{\hbar\omega})^2 + (\delta_{\mathcal{O}}^{\text{CC}})^2}, \quad (25)$$

where $\delta_{\mathcal{O}}^{\hbar\omega}$ is an estimate of the uncertainty related to the residual harmonic oscillator $\hbar\omega$ -dependence, while $\delta_{\mathcal{O}}^{\text{CC}}$ is an estimate of the coupled-cluster truncation uncertainty. For the latter, in case of the D/D calculations we take the difference from the T-1/D and D/D results, while in case of the T-1/D calculations, given that we do not have any higher order coupled-cluster calculation available, we take half of the above mentioned difference. More formally stated, the two uncertainties summed in quadrature are taken to be

$$\begin{aligned} \delta_{\mathcal{O}}^{\hbar\omega} &= \frac{\mathcal{O}(\hbar\omega_1) - \mathcal{O}(\hbar\omega_2)}{2}, \\ \delta_{\mathcal{O}}^{\text{CC}} &= \mathcal{O}^{\text{D/D}}(\hbar\omega_1) - \mathcal{O}^{\text{T-1/D}}(\hbar\omega_1) \end{aligned} \quad (26)$$

for the D/D calculations, and

$$\begin{aligned} \delta_{\mathcal{O}}^{\hbar\omega} &= \frac{\mathcal{O}(\hbar\omega_1) - \mathcal{O}(\hbar\omega_2)}{2}, \\ \delta_{\mathcal{O}}^{\text{CC}} &= 0.5 \cdot \left(\mathcal{O}^{\text{D/D}}(\hbar\omega_1) - \mathcal{O}^{\text{T-1/D}}(\hbar\omega_1) \right) \end{aligned} \quad (27)$$

for the T-1/D calculations. The values are computed for the maximum available model space size of $N_{\text{max}} = 14$, using two neighboring frequencies around the optimal value, namely $\hbar\omega_1 = 16$ MeV and $\hbar\omega_2 = 12$ MeV. The uncertainties of R_{skin} are obtained taking the correlation between R_p and R_n into account using standard covariance theory.

Clearly, this is a rough uncertainty estimate, but we find it sensible for the purpose of updating Ref. [1].

From Fig. 7, it is clear that the strong correlation between R_p , R_n and α_D , which was observed in [1], is confirmed, as well as we reinforce the fact that R_{skin} is almost constant with respect to the employed interaction. As done in Ref. [1], one can exploit the correlation among observables with the fact that the proton distribution radius is known experimentally, and from the intersection between the correlation band and the horizontal line, one can draw constraints on the neutron-skin thickness and the electric dipole polarizability. In Fig. 7 we do not explicitly show these constraints, but rather highlight the linear correlation bands and the experimental constraints with their corresponding uncertainty. With respect to Ref. [1], revisiting the calculations with leading triples, we obtain that the constraints on the dipole polarizability move from $2.19 \leq \alpha_D \leq 2.60 \text{ fm}^3$ to $1.92 \leq \alpha_D \leq 2.38 \text{ fm}^3$, thus getting closer to the experimental value of $2.07(22) \text{ fm}^3$ [60], while the constraints for the neutron-skin thickness go from $0.12 \leq R_{\text{skin}} \leq 0.15 \text{ fm}$ to $0.13 \leq R_{\text{skin}} \leq 0.16 \text{ fm}$, thus not varying much. Despite the fact that R_{skin} becomes smaller with triples for a given model space parameter set, the width of the neutron-skin thickness constraint, as well as the central value of R_{skin} are slightly increased with respect to [1]. This is due to a combination of facts: the use of symmetric correlation bands; the use of five instead of six [1] different interactions, and the use of optimal harmonic-oscillator frequencies, where the convergence in N_{max} is faster. The difference is anyway small and the updated ^{48}Ca study further establishes that the ab initio prediction of the neutron-skin thickness is much smaller than the values obtained from selected den-

sity functional theory calculations, shown in Fig. 7 by the diamonds. Thus, it is worth to reiterate that it is important to have a clean, as model-independent as possible, experimental determination of R_{skin} .

5 Conclusions

In this paper we review the recent progress made in the computation of electromagnetic response functions and related sum rules using a coupled-cluster theory formulation of the Lorentz integral transform method. We present photoabsorption cross sections of ^{16}O and ^{40}Ca , showing that we obtain a reasonable description of the experimental data already with two-body forces. We also review our calculations of the electric dipole polarizability, for which we use NN+3N Hamiltonians. We also present new results for the polarizability of ^{16}O and ^{48}Ca that include leading triples coupled-cluster correlations. For the ^{48}Ca case, we revisit our previous studies of correlations among the electric dipole polarizability, the neutron-, proton- and skin-radius. We show that correlations still hold and allow to draw improved predictions for the value of the polarizability, which is in better agreement with experiment, as well as for the neutron-skin thickness, for which we corroborate the earlier finding that ab initio theory predicts a smaller neutron skin than density functional theory.

Acknowledgments.— This work was supported by the Deutsche Forschungsgemeinschaft (DFG) through the Collaborative Research Center [The Low-Energy Frontier of the Standard Model (SFB 1044)]; by the Cluster of Excellence Precision Physics, Fundamental Interactions, and Structure of Matter (PRISMA⁺ EXC 2118/1) funded by DFG within the German Excellence Strategy (Project ID 39083149) and by the Office of Nuclear Physics, U.S. Department of Energy, under grants desc0018223 (NUCLEI SciDAC-4 collaboration) and by the Field Work Proposal ERKBP72 at Oak Ridge National Laboratory (ORNL). Computer time was provided by the Innovative and Novel Computational Impact on Theory and Experiment (INCITE) program. The new calculations presented in this work were also performed on “Mogon II” at Johannes Gutenberg-Universität in Mainz.

References

- G. Hagen, A. Ekström, C. Forssén, G. R. Jansen, W. Nazarewicz, T. Papenbrock, K. A. Wendt, S. Bacca, N. Barnea, B. Carlsson, C. Drischler, K. Hebeler, M. Hjorth-Jensen, M. Miorelli, G. Orlandini, A. Schwenk, and J. Simonis, *Nat. Phys.* **12**, 186 (2016).
- M. Goldhaber and E. Teller, *Phys. Rev.* **74**, 1046 (1948).
- H. Steinwedel and J. H. D. Jensen, *Z. Naturforsch.* **5A**, 413 (1950).
- A. Bracco, E. G. Lanza, and A. Tamii, *Prog. Part. Nucl. Phys.* **106**, 360 (2019).
- S. Weinberg, *Phys. Lett. B* **251**, 288 (1990).
- E. Epelbaum, H.-W. Hammer, and U.-G. Meißner, *Rev. Mod. Phys.* **81**, 1773 (2009).
- R. Machleidt and D. R. Entem, *Phys. Rep.* **503**, 1 (2011).
- E. Epelbaum and U.-G. Meißner, *Ann. Rev. Nucl. Part. Sci.* **62**, 159 (2012).
- R. B. Wiringa, V. G. J. Stoks, and R. Schiavilla, *Phys. Rev. C* **51**, 38 (1995).
- W. Leidemann and G. Orlandini, *Prog. Part. Nucl. Phys.* **68**, 158 (2013).
- S. Bacca and S. Pastore, *J. Phys. G: Nucl. Part. Phys.* **41**, 123002 (2014).
- K. Hebeler, J. D. Holt, J. Menéndez, and A. Schwenk, *Ann. Rev. Nucl. Part. Sci.* **65**, 457 (2015).
- M. Hjorth-Jensen, *Physics* **4**, 38 (2011).
- G. Hagen, G. R. Jansen, and T. Papenbrock, *Phys. Rev. Lett.* **117**, 172501 (2016).
- J. Simonis, S. R. Stroberg, K. Hebeler, J. D. Holt, and A. Schwenk, *Phys. Rev. C* **96**, 014303 (2017).
- T. D. Morris, J. Simonis, S. R. Stroberg, C. Stumpf, G. Hagen, J. D. Holt, G. R. Jansen, T. Papenbrock, R. Roth, and A. Schwenk, *Phys. Rev. Lett.* **120**, 152503 (2018).
- P. Gysbers, G. Hagen, J. D. Holt, G. R. Jansen, T. D. Morris, P. Navrátil, T. Papenbrock, S. Quaglioni, A. Schwenk, S. R. Stroberg, and K. A. Wendt, *Nat. Phys.* (2019), DOI:10.1038/s41567-019-0450-7, arXiv:1903.00047.
- G. Hagen, T. Papenbrock, M. Hjorth-Jensen, and D. J. Dean, *Rep. Prog. Phys.* **77**, 096302 (2014).
- V. D. Efros, W. Leidemann, and G. Orlandini, *Phys. Lett. B* **338**, 130 (1994).
- V. D. Efros, W. Leidemann, G. Orlandini, and N. Barnea, *J. Phys. G: Nucl. Part. Phys.* **34**, R459 (2007).
- S. Bacca, N. Barnea, G. Hagen, G. Orlandini, and T. Papenbrock, *Phys. Rev. Lett.* **111**, 122502 (2013).
- F. Coester and H. Kümmel, *Nucl. Phys.* **17**, 477 (1960).
- I. Shavitt and R. J. Bartlett, *Many-body Methods in Chemistry and Physics*, (Cambridge University Press, 2009).
- R. J. Bartlett and M. Musiał, *Rev. Mod. Phys.* **79**, 291 (2007).
- G. Hagen, T. Papenbrock, D. J. Dean, M. Hjorth-Jensen, and B. Velamuri Asokan, *Phys. Rev. C* **80**, 021306(R) (2009).
- V. D. Efros, W. Leidemann, and G. Orlandini, *Few-Body Syst.* **26**, 251 (1999).
- D. Andreasi, W. Leidemann, C. Reiß, and M. Schwamb, *Eur. Phys. J. A* **24**, 361 (2005).
- A. La Piana and W. Leidemann, *Nucl. Phys. A* **677**, 423 (2000).
- J. Golak, R. Skibiński, W. Glöckle, H. Kamada, A. Nogga, H. Witała, V. D. Efros, W. Leidemann, G. Orlandini, and E. L. Tomusiak, *Nucl. Phys. A* **707**, 365 (2002).
- S. Bacca, M. A. Marchisio, N. Barnea, W. Leidemann, and G. Orlandini, *Phys. Rev. Lett.* **89**, 052502 (2002).
- S. Bacca, N. Barnea, W. Leidemann, and G. Orlandini, *Phys. Rev. C* **69**, 057001 (2004).
- S. Bacca, H. Arenhövel, N. Barnea, W. Leidemann, and G. Orlandini, *Phys. Lett. B* **603**, 159 (2004).
- J. Erler, P. Klüpfel, and P.-G. Reinhard, *J. Phys. G: Nucl. Part. Phys.* **38**, 033101 (2011).
- T. Nakatsukasa, *Prog. Theor. Exp. Phys.*, 01A207 (2012).
- J. Piekarewicz, B. K. Agrawal, G. Colò, W. Nazarewicz, N. Paar, P.-G. Reinhard, X. Roca-Maza, and D. Vretenar, *Phys. Rev. C* **85**, 041302(R) (2012).
- X. Roca-Maza and N. Paar, *Prog. Part. Nucl. Phys.* **101**, 96 (2018).

37. D. R. Entem and R. Machleidt, Phys. Rev. C **68**, 041001(R) (2003).
38. S. Bogner, R. J. Furnstahl, and R. J. Perry, Phys. Rev. C **75**, 061001(R) (2007).
39. K. Hebeler, S. K. Bogner, R. J. Furnstahl, A. Nogga, and A. Schwenk, Phys. Rev. C, **83**, 031301(R) (2011).
40. A. Ekström, G. R. Jansen, K. A. Wendt, G. Hagen, T. Papenbrock, B. D. Carlsson, C. Forssén, M. Hjorth-Jensen, P. Navrátil, and W. Nazarewicz, Phys. Rev. C **91**, 051301(R) (2015).
41. A. Calci and R. Roth, Phys. Rev. C **94**, 014322 (2016).
42. G. Hagen, T. Papenbrock, D. J. Dean, A. Schwenk, A. Nogga, M. Wloch, and P. Piecuch, Phys. Rev. C **76** 034302 (2007).
43. R. Roth, S. Binder, K. Vobig, A. Calci, J. Langhammer, and P. Navrátil, Phys. Rev. Lett. **109** 052501 (2012).
44. D. Gazit, N. Barnea, S. Bacca, W. Leidemann, and G. Orlandini, Phys. Rev. C **74**, 061001(R) (2006).
45. N. Barnea, W. Leidemann, and G. Orlandini, Phys. Rev. C **61**, 054001 (2000).
46. N. Barnea, W. Leidemann, and G. Orlandini, Nucl. Phys. A **693**, 565 (2001).
47. Yu. M. Arkatov *et al.*, Yad. Konst. **4**, 55 (1979).
48. R. Raut, W. Tornow, M. W. Ahmed, A. S. Crowell, J. H. Kelley, G. Rusev, S. C. Stave, and A. P. Tonchev, Phys. Rev. Lett. **108**, 042502 (2012).
49. W. Tornow, J. H. Kelley, R. Raut, G. Rusev, A. P. Tonchev, M. W. Ahmed, A. S. Crowell, and S. C. Stave, Phys. Rev. C **85**, 061001(R) (2012).
50. S. Nakayama *et al.*, Phys. Rev. C **76**, 021305(R) (2007).
51. T. Shima, S. Naito, Y. Nagai, T. Baba, K. Tamura, T. Takahashi, T. Kii, H. Ohgaki, and H. Toyokawa, Phys. Rev. C **72**, 044004 (2005).
52. J. Ahrens, H. Borchert, K. H. Czock, H. B. Eppler, H. Gimm, H. Gundry, M. Kröning, P. Riehn, G. Sita Ram, A. Zieger, and B. Ziegler, Nucl. Phys. A **251**, 479 (1975).
53. B. S. Ishkhanov and V. N. Orlin, Phys. At. Nucl. **67**, 920 (2004).
54. A. Leistenschneider *et al.*, Phys. Rev. Lett. **86**, 5442 (2001).
55. S. Bacca, N. Barnea, G. Hagen, M. Miorelli, G. Orlandini, and T. Papenbrock, Phys. Rev. C **90**, 064619 (2014).
56. M. Miorelli, S. Bacca, N. Barnea, G. Hagen, G. R. Jansen, G. Orlandini, and T. Papenbrock, Phys. Rev. C **94**, 034317 (2016).
57. C. Lanczos, J. Res. Natl. Bur. Stand. **45**, 255 (1950).
58. I. Angeli and K. P. Marinova, At. Data Nucl. Data Tables **99**, 69 (2013).
59. M. Miorelli, S. Bacca, G. Hagen, and T. Papenbrock, Phys. Rev. C **98**, 014324 (2018).
60. J. Birkhan, M. Miorelli, S. Bacca, S. Bassauer, C. A. Bertulani, G. Hagen, H. Matsubara, P. von Neumann-Cosel, T. Papenbrock, N. Pietralla, V. Yu. Ponomarev, A. Richter, A. Schwenk, and A. Tamii, Phys. Rev. Lett., **118**, 252501 (2017).
61. Y. S. Lee, S. A. Kucharski, and R. J. Bartlett, J. Chem. Phys. **81**, 5906 (1984).
62. J. D. Watts and R. J. Bartlett, Chem. Phys. Lett. **233**, 81 (1995).
63. G. R. Jansen, M. D. Schuster, A. Signoracci, G. Hagen, and P. Navrátil, Phys. Rev. C **94**, 011301(R) (2016).
64. F. Raimondi and C. Barbieri, arXiv:1811.07163.
65. C. J. Horowitz, K. S. Kumar, and R. Michaels, Eur. Phys. J. A **50**, 48 (2014).
66. S. Abrahamyan *et al.*, Phys. Rev. Lett. **108**, 112502 (2012).
67. M. Thiel, D. Becker, M. Ferretti, K. Kumar, and C. Sienti, EPJ Web Conf. **73**, 07007 (2014).